To appear in J. Mech. Phys. Solids (2010)

MODELING ADIABATIC SHEAR FAILURE FROM ENERGY CONSIDERATIONS

M. Dolinski, D. Rittel[1] and A. Dorogoy
Faculty of Mechanical Engineering
Technion, 32000 Haifa
Israel

ABSTRACT
The numerical simulation of dynamic structural failure by localized shear is quite complex in terms of constitutive models and choice of adequate failure criteria, along with a pronounced mesh-sensitivity. As a result, the existing numerical procedures are usually quite sophisticated, so that their application for design purposes is still limited. This study is based on the implementation of a simple energy-based criterion which was developed on experimental considerations (Rittel, et al., 2006), and uses a minimal number of adjustable parameters. According to this criterion, a material point starts to fail when the total strain energy density reaches a critical value. Thereafter, the strength of the element decreases gradually to zero to mimic the actual structural behavior. The criterion was embedded into commercial finite element software, and tested by simulating numerically four typical high-rate experiments. The first is the dynamic torsion test of a tubular specimen. The second concerns the failure mode transition in mode II fracture of an edge crack in plain strain. The last two involve dynamic shear localization under high rate compression of a cylindrical and a shear compression specimen. A very good adequation was found both qualitatively and quantitatively. Qualitatively, in terms of failure path selection, and quantitatively in terms of local strains, temperatures and critical impact velocity. The proposed approach is enticing from an engineering perspective aimed at predicting the onset and propagation of dynamic shear localization in actual structures.

Keywords: adiabatic shear, energy, failure, modeling, failure mode transition

[1] Corresponding author: *merittel@technion.ac.il*

1. Introduction

Adiabatic shear failure is a well documented dynamic failure mode in which failure proceeds by shear localization in a narrow plane (Bai and Dodd, 1992; Tresca, 1879), referred to as an adiabatic shear band (ASB). This phenomenon is quite well documented from a microstructural point of view, and a variety of characteristic microstructures has been reported, whose common point is that the material inside the shear band almost always undergoes dynamic recrystallization (Andrade, et al., 1994; Chichili, et al., 2004; Meyers, et al., 1996; Meyers, et al., 2000; Toth, et al., 2000). From a mechanical point of view, characteristic experiments are more scarce, with the noticeable exception of Marchand and Duffy's work (1988) as well as Kalthoff's experiments on dynamic fracture (1988), all of which involve shear band formation as the main failure mode. Modeling ASB is a very complex task in many respects. This comes from the fact that the ASB is considered as a material instability occurring in no time, with a marked influence of thermomechanical coupling effects (Bai and Dodd, 1992; Molinari and Clifton, 1987; Wright, 2002; Zener and Hollomon, 1944). Analytical models based on a geometrical or thermal perturbation have been proposed, such as the classical work of Molinari and Clifton (1987), which rely on the well accepted model of Zener and Hollomon (1944) about the competition between strain-rate hardening and thermal softening. Numerical modeling of ASB may be extremely complex as it requires a physical criterion for the onset of shear localization and sometimes ad-hoc constitutive models for the shear band material itself. Another pathological problem of shear localization is the well-known mesh-sensitivity of the problem which may lead to different results as to the width of the band (see also the analytical work of Merzer (1982). Among the many numerical models that were published, we will mention those which are closely related to experimental results or physical phenomena in the band. These include the work of Zhou et al. (Zhou, et al., 1996a; 1996b) who modeled Kalthoff's experiments on Maraging steel (1988), with the failure mode transition that occurs during mode II impact of a notched plate. In these experiments, failure proceeds at a 70º angle at low impact velocities, which then becomes a 0º angle (ASB) at higher impact velocities. This failure mode transition from opening to adiabatic shear was also reported for amorphous polymers (Ravi-Chandar, 1995; Rittel, 1998). To successfully model their experiments including the shear band propagation velocity, Zhou et al. (Zhou, et al., 1996a; 1996b) used

specially devised failure criteria (failure strain) and constitutive models which they implemented in a commercial finite element code. Slightly earlier, Needleman and Tvergaard (1995) presented a numerical model of the same problem. Two competing failure criteria were implemented, namely brittle cleavage and ductile thermal softening and void growth. These authors concluded that thermal softening is an important component of the shear localization process. Batra and Lear (2004) modeled the failure mode transition of 4340 steel plates using a critical strain criterion for ASB formation and a maximum principal stress criterion for brittle fracture. The value of the critical strain was set arbitrarily to 0.5 and damage evolution in the band was interpreted as porosity. Porosity in the adiabatic shear band was also accounted for by McVeigh et al. (2007), to model damage evolution in the band. In this context, one should also mention the work of Medyanik et al. (2007) who explicitly introduced dynamic recrystallization in the shear band as a form of post-localization damage. We note in passing that to each of these considerations, namely width of the shear band and specific damage weakening mechanisms (dynamic recrystallization and microvoids), one must add additional empirical equations that describe the evolution of the damage in the band. Consequently, numerical modeling of adiabatic shear failure with its specific thermal and mechanical features has become a very complicated task, for which even if the results seem to qualitatively reproduce some experiments, the range of practical applications (design) is still limited. In parallel, the engineering community has a great need for simple modeling tools that would allow prediction of the evolution of adiabatic shear failure in an impulsively loaded structure.

In the recent years, a different approach has emerged concerning ASB formation (Rittel, et al., 2006). To summarize its essential features, this approach considers thermal softening as a minor player in the shear band formation, while proposing that the dynamically stored energy of cold work (Bever, et al., 1973; Taylor and Quinney, 1934) is the driving force for strain localization. The precise identification of the stored energy of cold work requires an accurate measurement of the temperature rise of the specimen. However, in their original work, Rittel et al. (2006) measured the total strain energy density, showing it remained constant in various thermomechanical conditions, thus leading to the conclusion about the key role of the stored energy component. A somewhat parallel approach was reported in the tribological context, in which observations of a fine recrystallized structure were first made in a Ti6Al4V

alloy (Sauger, et al., 2000). These observations led to a model based on the dissipated energy as the driving force for the tribological failure mechanism (Fouvry, et al., 2003). A direct connection with the microstructure of the dynamically deformed material was established by Rittel et al. (2008) who identified early dynamic recrystallization as a potent factor for local softening of an otherwise strain-hardening material. Dynamic recrystallization is deemed to be driven by the stored energy of cold work. This observation bears an additional implication for the phenomenon, in the sense that dynamic recrystallization develops gradually during the plastically stable phase of the material, so that the instability approach (Zener and Hollomon, 1944) may not be needed in that case. These two works (Rittel, et al., 2008; 2006) propose a different look on ASB formation in which the physics of failure comprises no instability (rather a gradual solid transformation), with a minor thermal activation component, for which a dynamic strain-energy density criterion is sufficient to describe the onset of failure. When such an approach is adopted, the problem of modeling the initiation and propagation of ASB becomes greatly simplified even if the mesh-dependence has not disappeared yet.

This paper describes new results coming from the implementation of energy considerations as a dynamic failure criterion by adiabatic shear banding. Four experimental cases are analyzed, namely Marchand and Duffy's work (1988), the failure mode transition (Kalthoff, 1988), followed by the impacted cylinder and finally the shear compression specimen (SCS) (Rittel, et al., 2002). It is important to note at this stage that a single and same criterion is used throughout this work to model the initiation and propagation phases of the adiabatic shear band in a variety of experimental configurations.

The paper is organized as follows: first we present the failure criterion and its implementation as well as the identification of its constitutive parameters. Care is paid to the criterion and the damage evolution after the critical conditions are reached. Next, we report and discuss 4 numerical test cases which correspond to actual experiments, followed by a discussion and a concluding section.

2. Energy failure criterion and its implementation

The failure criterion consists of a critical level of the total strain energy density W_{crit} reached in *each element*, given by:

$$W_{crit} = \int_0^{\alpha} \sigma_{ij} d\varepsilon_{ij} \qquad (1)$$

Where σ and ε are the stress and strain tensor components respectively, noting that here the contribution of the elastic strains is included to match the original work of Rittel et al (2006). The upper integration limit α is selected as the level of strain at which the structural strength starts to deteriorate, $\tilde{\varepsilon}_{eq}^{crit}$. From this point, the element starts to fail gradually, rather than abruptly, according to:

$$\tilde{\sigma}_{eq} = \tilde{\sigma}_{eq}^{*} * \left(1 - D^{b}\right) \qquad (2)$$

Where $\tilde{\sigma}_{eq}^{*}$ is the current equivalent stress level at a given equivalent strain $\tilde{\varepsilon}_{eq} \geq \tilde{\varepsilon}_{eq}^{crit}$, D is the level of damage in the element and b is an exponent. The damage level is given by:

$$D = \frac{W - W_{crit}}{W_{frac} - W_{crit}} \qquad (3)$$

Note that $W_{frac} = W(\varepsilon_{eq}, \sigma_{eq} = 0)$, excluding of course the origin of the stress-strain curve. In other words, W_{frac} is the strain energy density when the stress drops to zero. The failure criterion is illustrated graphically in Figure 1.

This criterion was implemented via a user-subroutine (VUSDFLD) in the commercial finite element code Abaqus explicit (2007), see supplementary material.

It is important to note that this criterion was used to gradually delete elements, resulting *de-facto* in the propagation of the shear band as an increasing number of neighboring elements gradually meet the proposed criterion. In other words, both the initiation and the propagation phases of the shear band were modeled using the same criterion.

3. Numerical test cases for the energy criterion.

In order to test the viability of the suggested energy criterion, four numerical test cases were solved. The purpose is to compare the numerical and experimental results, both qualitatively and quantitatively. In all these test cases, a dynamic load is applied

to a specimen that fails due to dynamic fracture or adiabatic shear banding. The first test case (1) is the high rate torsion of thin-walled cylindrical specimens. It was chosen because the dominant load is shear and there are thorough experimental results for a quantitative comparison. These include local strains and temperature, as well as global mechanical data. The second test case (2) is the dynamic mode II fracture of a plate containing an edge crack. The experimental results of Kalthoff (1988) show a failure mode transition (brittle to ASB) at a particular impact velocity. The purpose of the numerical simulations is to reproduce the experimental behavior in terms of the transition velocity and resulting fracture path. Finally, two test cases (3-4) of two different specimens (cylinder and shear compression specimen, SCS) made of the same material were simulated, with emphasis on the failure path.

The commercial finite elements software Abaqus/Explicit v 6.8-2 (2007) was used for the simulations. In all the four test cases the energy criterion was implemented in a "user subroutine" called VUSDFLD. In three of the test cases (1, 3 and 4) the energy criterion was used alone, while for test case (2) an additional failure criterion for brittle fracture was added. However, the two criteria were applied simultaneously in the user-subroutine, and whichever was first fulfilled dictated the failure mode.

With exception of test case (2), Johnson-Cook (1985) constitutive material model was used (referred to as JC in the sequel):

$$\sigma = \left[A + B(\varepsilon_p)^n \right] \left(1 + C \ln \frac{\dot{\varepsilon}}{\dot{\varepsilon}_R} \right) \left[1 - \left(\frac{T - T_0}{T_m - T_0} \right)^m \right] \qquad (4)$$

Where A, B, C, n, m are material constants for strain-rate hardening, strain-hardening and thermal softening effects respectively, while ε_p is the plastic equivalent strain, $\dot{\varepsilon}$ is the strain rate, $\dot{\varepsilon}_R$ is the reference strain rate, T_0 is the initial temperature and T_m is the material melting temperature.

It should be noted, that the user-subroutine VUSDFLD does not directly accept JC's equation as an input. Therefore, plastic stress-strain curves were generated from eqn. (4) for various temperatures and strain rates as an input file.

For the second test case, mode II fracture of a plate containing an edge crack, we used experimental data generated in our laboratory for Maraging 250 steel (Zisso, 2006). The material properties and the energy criterion parameters for each test case are summarized in Table 1.

The damage model parameters were determined as follows:

- Determination of the JC constitutive parameters (or plastic behavior), which reproduce numerically the experimental dynamic stress-strain curves.
- Integration of the experimental stress-strain curves (eqn. (1)) to provide W_{crit}.
- Empirical determination of W_{frac} and b to numerically reproduce the experimental average shear stress – shear strain curves.
- Performing a mesh convergence test in which three different mesh sizes were iteratively used. First, a preliminary assessment was made using a given (medium) mesh. Then the same analysis was repeated with two other meshes: coarser and finer. Convergence was deemed to be fulfilled if the medium and fine meshes both gave close results for the average stress-strain curve and failure path.

3.1 *Torsion of thin walled cylindrical specimens (Marchand and Duffy, 1988)*

3.1.1. Geometry

A thin walled cylindrical specimen was analyzed. The specimen's dimensions are the same as those of Marchand and Duffy (1988), see Figure S1 in supplementary material. A circumferential geometrical imperfection with a radius of 9[mm] was introduced in the middle of the gauge. This groove was used in order to enforce the formation of the shear band in the middle of the gauge-section. Note that Marchand and Duffy (1988) also mentioned the presence of a small geometrical imperfection (wall thickness). This slight geometrical imperfection is also discussed in the work of Molinari and Clifton (1987).

3.1.2 Boundary conditions and loads

A velocity boundary condition was applied on one of the specimen's hexagonal part, while the opposite face was constrained as shown in Figure 2. These boundary conditions simulate a split Hopkinson torsion bar test. The applied velocity profile (Table 2) was selected to match the experimental conditions of Marchand and Duffy's experiments (1988).

3.1.3 Material

All specimens were made of HY-100. The JC coefficients reported for this material (Shi and Liu, 2004) were slightly modified to obtain the shear stress-shear strain curve given by Marchand and Duffy (1988). This curve represents an average over a line across the gauge-section along the axis of the cylinder. The elastic parameters, material properties, JC parameters and the failure criterion parameters are all summarized in Table 1.

3.1.4 Mesh

As mentioned previously, three meshes (coarse, medium and fine) were generated with hexahedral elements of type C3D8R. The medium mesh, for which results are presented in the sequel, comprises a total of 31900 elements, with 12 elements across the gauge-section (Figure 2).

3.1.5 Numerical results and comparison to experiments

The average shear stress and strain which were calculated in the gauge-section for the 3 different mesh sizes, are shown in Figure 3. The experimental curve of Marchand and Duffy (1988) is also shown for comparison. It can be observed that the curves are rather similar indicating a satisfactory level of convergence.

The distorted specimen is shown in Figure 4 at selected time intervals, namely t=150[μs], 250[μs], and 280[μs]. Those pictures describe the evolution of the damage, noting that at t=150[μs] (Figure 4a) the specimen is almost reaching its critical condition for failure. Failure develops as shown for the two time intervals t=250[μs], and 280[μs] (Figures 4b and 4c). The highest value of the strain energy density (on an element base), Figure 4a, is $W = 242\left[MJ/m^3\right]$. This value is slightly smaller than W_{crit} which means that the structure is not damaged yet, even though the deformations are already inhomogeneous. This observed strain localization is due to the circumferential groove. The maximal local shear strain inside the groove is $\gamma_{loc} = 0.41$ while the average shear strain across the groove is $\gamma_{nom} = 0.26$. In Figure 4b, the highest strain energy of the specimen is $W = 498\left[MJ/m^3\right]$, and $\gamma_{loc} = 0.80$ while

$\gamma_{nom} = 0.41$. Here, one can observe that strain localization clearly occurs. The specimen of Figure 4c has a highest value of $W = 579\left[MJ/m^3\right]$, with $\gamma_{loc} = 1.07$ and $\gamma_{nom} = 0.43$. The localization is clearer, and it appears to be confined to a single row of elements. The average shear strain from the previous time step is barely changed but the local shear strain has increased significantly.

It should be noted that in our simulations, the maximal shear strain was approximately $\gamma_{loc}^{\max} \approx 1.00$. We did not pursue the calculations beyond that value to avoid heavily distorted elements which impair the accuracy of the calculations irrespective of mesh size and requires remeshing.

A global (averaged nominal) and local (shear band) stress-strain curve are shown in Figure 5. These curves are very similar up to $\gamma_{nom} \approx 0.40$, and beyond this nominal strain level the strain grows dramatically in the shear band, causing overall structural unloading as shown by the averaged nominal curve.

One can also compare the calculated local strain levels at a nominal strain $\gamma_{nom} = 0.36$ to the experimental results of Marchand and Duffy (1988). The numerical results at $t = 210\left[\mu s\right]$ are: $\gamma_{nom} = 0.36$, $\gamma_{loc} = 0.6$, , and $\tau_{max} = 570[\text{MPa}]$. The experimental results are: $\gamma_{nom} = 0.36$ and $\gamma_{loc} = 0.9$ without specification of the time at which the picture is taken or the specific stress-strain curve for this particular experiment. Yet, the trend observed in the calculations definitely captures the experimental trend of high local strains.

Marchand and Duffy (1988) also measured the local temperature changes on the specimen's surface using a high speed infrared radiometer. The numerically calculated temperature on the outer shell as a function of time and position across the gauge-section is shown in Figure 6. A calculated maximal temperature rise of 150ºC is obtained at t= 280[μs]. This temperature is observed, as expected, at the center of the gauge-section where localization occurs. The temperature envelope gets narrower in time, showing a very similar trend to the reported experimental results. It can be noticed that a steep thermal gradient develops beyond t=230[μs]. This time corresponds precisely to the time at which the shear band starts to develop (criterion reached). The maximal calculated temperature rise is 150ºC and is obtained when the stress drops to 2/3 of its maximal value. Note that a thermomechanical conversion

factor of $\beta_{\text{int}} = 0.9$ was assumed in the calculation while this factor actually evolves with the strain (Mason, et al., 1994; Rittel, 1999) .

A value of 200ºC is reported experimentally for a stress drop down to half its maximal value. Extrapolating the numerically calculated temperature rise to the same level of decrease of the experimental nominal stress yields a temperature rise of 210ºC. This value is very close to the reported experimental value.

3.2 Dynamic mode II fracture of a plate containing a blunt edge crack (Kalthoff, 1988)

The purpose of this model is to reproduce the dynamic mode II failure transition which was observed experimentally by Kalthoff (1988) and also by Zhou et al. (Zhou, et al., 1996a; 1996b).

3.2.1. Geometry

The specimen geometry and dimensions are shown in Figure 7. The specimen contains a single notch with a root radius of 200[μm]. A two-dimensional, plane strain analysis was conducted.

3.2.2 Boundary conditions and loads

The striker is not included in the numerical model, and a velocity boundary condition is applied on the part of the edge where the projectile is impacting the specimen (Figure 7). A calculation of the mechanical impedance mismatch between a 12.7[mm] diameter Maraging steel projectile and the plate specimen was carried out. This calculation shows that the ratio of impedances between the specimen and the projectile is approximately 0.9. This factor was used to properly apply the boundary velocity condition due to the actual projectile's velocity. Note that a similar ratio was obtained by Batra and Ravinsankar (2000).

3.2.3 Material

Although both Kalthoff (1988) and Zhou et al. (Zhou, et al., 1996a; 1996b) investigated C300 Maraging steel, we used our available experimental database for Maraging 250 steel (Zisso, 2006), based on the fact that the two grades of steel are not markedly different. The elastic and plastic parameters, material properties as well as the energy failure criterion are listed in Table 1. Here, instead of a JC constitutive material behavior, the stress is given as a function of plastic strain, strain rate and temperature. The strain rate and temperature dependence of the strength were determined as follows. The static yield stress is 2050[MPa], and the flow stress at $\varepsilon_p = 0.15$ is 2100[MPa] (Zisso, 2006). A strain rate of $\dot{\varepsilon} = 3000\left[s^{-1}\right]$ causes a rise of 150[MPa] to both of them (Zisso, 2006). We then assumed that at $\dot{\varepsilon} = 10000\left[s^{-1}\right]$, the stress levels are increased by 350[MPa]. On the other hand, we also assumed that for $\Delta T = 100^{\circ}$, the stress levels drop by 200[MPa]. It was also observed that the dynamic tensile strength is highly rate-dependent as shown in Figure 8 (Zisso, 2006). The input to Abaqus should be in the form a table of failure strength versus strain-rate, hence the impact velocity values were approximately converted into representative strain-rates near the notch-tip. The above mentioned strength data was first used to calculate a representative (range of) notch-tip strain-rates corresponding to each impact velocity, without any failure criterion. Next, we used the data of Figure 8 (dynamic tensile failure stress at each strain rate) to establish the correspondence between impact velocity and tensile fracture stress to be used in the simulations. One should realize that this estimation procedure is of an approximate nature, yet it is more physical than simply extrapolating the tensile failure stress (Figure 8) to the very high strain rates in the vicinity of the notch-tip. Such a procedure would result in very high and probably unphysical values of the failure stress.

The brittle fracture criterion was thus selected as the maximum normal stress $\sigma_{\theta\theta}^{\max}$.

Table 3 summarizes the values of the tensile failure strength as a function of the impact velocity.

The data for the ductile failure criterion was obtained from dynamic compression tests of cylinders, for which adiabatic shear failure was observed (Zisso, 2006). It was found that the parameter W_{crit} is not rate-dependent.

3.2.4 Mesh

Two dimensional linear quadrilateral, plane strain elements of type CPE4R were used. The medium mesh, for which results are presented in the sequel, comprises a total of 32923 elements, with 12 elements on the notch tip. This mesh was found to be converged, as discussed in Section 3.

3.2.5 Numerical results and comparison to experiments

The maximum normal stress map in the neighborhood of the crack tip for an impact velocity of 17[m/s] is plotted in Figure 9. The values at time t=10[μs] and t=12[μs] are shown in Figure 9a and 9b correspondingly. At t≈11[μs], the brittle fracture criterion is reached, with a value of $\sigma_{\theta\theta}^{\max} = 3056[MPa]$, which is close to the selected critical value of 3200[*MPa*]. A crack is seen to propagate in Figure 9b at an inclined angle of ~ 70°, similar to what was reported in the experiments.

The energy criterion values in the neighborhood of the crack tip for an impact velocity of 18[m/s] are plotted in Figure 10. For this impact velocity, the failure mode is shear localization rather than brittle fracture. The values at time t=18[μs] and t=20[μs] are shown in Figure 10a and 10b respectively. At t≈18[μs], the (ductile) energy failure criterion is already met, and the structure has reached a state of localized shear. The physical picture is different from that shown in Figure 9 since the failure which starts developing at t≈20[μs] on the bottom part of the notch-tip, propagates parallel to the original notch.

Typical results for an impact velocity of 25[m/s] are shown in Figure 11. The shear band initiates at t≈13[μs], much earlier than at an impact velocity of 18[m/s]. The shear band keeps propagating until a time of t≈70[μs], at which a different picture emerges. The brittle failure criterion is met again, and a crack is seen to emanate from the shear band at $\theta \approx -30^{\circ}$. The shape of the maximum principal stress contour around the crack clearly indicates a mode I crack. Note that a similar observation of a crack emanating from a shear band tip was reported by Zhou et al. (Zhou, et al., 1996a; 1996b). At an impact velocity of 25[m/s], these authors report an average shear band velocity of 595[m/s]. The present simulation predicts an average shear band propagation velocity of 430[m/s]. The calculated velocity is rather close to the measured one, taking into account the difference in specimen geometries and exact

material grade. The calculations also show that the shear band velocity increases as the impact velocity increase, but this point was not further investigated.
Considering the projectile/specimen impedance mismatch (0.9), the failure mode transition which occurs at an applied boundary velocity of 18[m/s] corresponds to a striker velocity of 20[m/s]. This value is the same as the velocity reported by Kalthoff (Kalthoff, 1988) and by Zhou et al. (Zhou, et al., 1996a; 1996b).

3.3 Dynamic fracture of magnesium-aluminum alloy (AM50) specimens

This section reports 3D numerical simulations of two specimen geometries made of magnesium-aluminum alloy (AM50) (Rittel, et al., 2006). The specimens were tested in a Split Hopkinson Pressure Bar (Kolsky, 1949).
The interesting point of the section lies in the fact that two completely different specimen geometries, each with a specific failure mode, are successfully simulated with a very similar set of failure criterion parameters.

3.3.1 Axially impacted cylinder

3.3.1.1. Geometry

The cylindrical specimen's dimensions are Ø6 x 6 [mm].

3.3.1.2 Boundary conditions and loads

The whole experimental setup (Hopkinson bars and specimen) was modeled (see Figure S2 in supplementary material). The incident bar is subjected to a velocity boundary condition whose profile is given in Table 4. Frictional contact conditions were assumed between the specimen and the bars with a Coulomb friction coefficient of $\mu = 0.5$. This coefficient value best fits the experimental results (slight barreling of the cylindrical shape).
The two bars are made of Maraging 300 steel which have elastic coefficients of E=210[GPa], ν=0.3 and ρ=7800[Kg / m^3].

3.3.1.3 Material

The specimens are made of magnesium-aluminum alloy (AM50) whose physical properties, elastic parameters, plastic Johnson-Cook coefficients and failure criterion parameters are summarized in Table 1. The mechanical properties were determined by Wang (2007).

3.3.1.4 Mesh

The mesh comprises 79856 3D linear hexahedral elements of type C3D8R, out of which 66640 elements for the specimen. This mesh was found to be converged, as discussed in Section 3.

3.3.1.5 Numerical results and comparison to experiments

A typical cross section of the deformed specimen is shown in Figure 12a. The experimental tests reveal that the AM50 specimen usually fails by formation of a conical plug whose outer boundaries are adiabatic shear planes, as shown in Figure 12b. One can notice the high degree of similarity of the failure paths that are either predicted numerically or observed experimentally.

3.3.2 Shear Compression Specimen

The shear compression specimen (SCS) was initially designed to enforce a dominant state of shear in the specimen gauge-section, at high strain rates and to avoid plastic instability at large strains (Rittel, et al., 2002).

3.3.2.1. Geometry

Because of the symmetry of the SCS, just one-half of the specimen was modeled. The half meshed specimen is shown in Figure 13 (Dorogoy and Rittel, 2005).

3.3.2.2 Boundary conditions and loads

Since most of the deformation occurs in the gauge section of the SCS, friction with the bars is less relevant. Therefore, the model just includes the specimen with application of a velocity profile (Table 5), on one side while the other side is constrained. The boundary conditions are shown in Figure 13. The reported results were collected on a line passing at mid-gauge height.

3.3.2.3 Material

The material parameters are listed in Table 1. The parameters used here are quite similar to those used in the previous simulation. Minor differences in mechanical properties were introduced in order to reproduce more accurately the reported SCS experimental results (Rittel, et al., 2006).

3.3.2.4 Mesh

The medium mesh comprised 56007 linear hexahedral elements of type C3D8R and 1203 linear wedge elements of type. Here too, this mesh was found to be converged, as discussed in Section 3.

3.3.2.5 Numerical results and comparison to experiments

Figure 14 shows the failure pattern in the specimen. A shear band starts on each side of the fillet and propagates inward (14a). The two different bands finally bridge through the gauge height and separation occurs by a short connecting slant fracture segment (14b).

This kind of failure was frequently observed in experimental tests of AM50 specimens. Figure 15 shows such a specimen for which fracture was for its most part located in the upper and lower fillets of the gauge section, with a short slant fracture connecting the two planes. A high level of similarity between the present numerical results and the experimental observations can be noted.

Here, one must mention that various degrees of mesh refinement were observed to slightly affect the angle and position of the slant fracture segment without changing at all the overall picture of the failure mechanism. Incidentally, the precise location of

this segment was observed to vary in several test specimens so that the importance of this variability cannot be further discussed in the present context.

4. Discussion

The presented work is based on the implementation of a simple energy criterion to represent the onset of localized (adiabatic shear) failure in an impacted structure, in the spirit of Rittel et al's. suggestion (2006). The onset of failure is modeled by reaching of a critical level of strain energy density in a specific element. This specific value can be measured experimentally. However, the structure (element) does not fail completely at that stage and a damage evolution procedure is added to represent the fact that the structure retains some of its load-bearing capacity in spite of the localization, similar to what is actually observed.

The proposed approach is simpler than the usual ones, which include a detailed modeling of the softening and failure mechanisms for which many physical parameters are often missing. It is nevertheless quite macroscopic in the sense that the fine physics underlying shear localization, such as the actual width of the shear band are not represented here. Rather, the latter corresponds to the selected mesh, thereby displaying the usual mesh-dependence pathology. Therefore, instead of attempting to model the actual microstructural and mechanical evolutions that lead to final collapse, we deliberately adopt a simplified criterion in which the shear band is formed once a critical level of strain energy density has been reached, and gradual failure ensues as described by a macroscopic generic damage law. Again, one must keep in mind the physical connection between energy and microstructural evolutions, which cannot be simply established from strain considerations for example.

With regards to the failure model itself, it was observed that except for HY-100, the parameter b was always equal to 1. Similarly, except for 250 Maraging steel, we found that $W_{fract} \approx 3W_{crit}$, however one cannot claim that this kind of observations is universal, and additional work is needed to verify this point.

The proposed modeling approach was applied to the simulation of four distinct dynamic failure experiments, for which the results showed qualitative and sometimes quantitative similarities, in a systematic benchmark that was not previously attempted to the best of our knowledge.

Marchand and Duffy's experiment (1988) was qualitatively well simulated using parameters that were extracted from the experiments. The simulation reproduced the various stages of the localization process with a correct prediction of the local temperatures and strains. Another interesting outcome was the numerical calculation of the local stress-strain curve for the shear band, and its relation with the macroscopic one (Figure 5).

Simulations of Kalthoff's experiment (1988) on the failure mode transition, again inspired from measured parameters for this (similar) material, rendered a very realistic picture of the phenomenon. It will be noted here that 2 competing criteria were used, and the rate sensitivity of the dynamic tensile strength was observed to be responsible for the shift in failure mode. The qualitative evolution of a shear band into an opening crack was correctly rendered at high impact velocities, and the impact velocity of 20[m/s] was also correctly predicted to cause the transition. Moreover, in spite of its simplicity, the model successfully reproduced the propagation velocity of the shear band, to the right order of magnitude.

Finally, one specific material (AM50) was modeled in two different specimen geometries, both exhibiting shear localization, with a different geometrical pattern. In both cases, the fracture paths were successfully reproduced, including even the small slant fracture segment which connects the shear bands in each fillet of the SCS's gauge section.

Consequently, it is felt that simulations of the kind reported in this paper, although approximate in their physical representation, have nevertheless a strong potential to simulate actual engineering dynamic failures, with a high degree of accuracy and simplicity.

5. **Conclusions**

- The proposed macroscopic approach to model dynamic shear localization is a viable alternative to more sophisticated models for which the number of adjustable parameters may become large.
- The energy density criterion is successful in reproducing several quantitative and qualitative salient aspects of dynamic failure experiments.

- It was also shown that this criterion can be matched with other criteria to reproduce quite faithfully complex experimental observations such as dynamic failure mode transition (Kalthoff, 1988).
- The rate sensitivity of the tensile flow stress of Maraging steel was found to be instrumental in dictating the failure mode transition.
- The presented approach is quite enticing from an engineering design perspective, when one wants to obtain a clear feeling for the potential occurrence of localized shear failure.

Acknowledgement: The support of Israel Science Foundation (grant 2011362) is kindly acknowledged.

BIBLIOGRAPHY

Abaqus, 2007. Finite Element Package (explicit). Dassault Systemes Providence, RI.

Andrade, U., Meyers, M.A., Vecchio, K.S., Chokshi, A.H., 1994. Dynamic recrystallization in high strain, high strain rate plastic deformation of copper Acta Metall. Mater. 42 (9), 3183-3195.

Bai, Y., Dodd, B., 1992. Shear Localization: Occurrence, Theories, and Applications. Pergamon Press, Oxford, UK.

Batra, R.C., Lear, M.H., 2004. Simulation of brittle and ductile fracture in an impact loaded prenotched plate. International Journal of Fracture 126 (2), 179-203.

Batra, R.C., Ravinsankar, M.V.S., 2000. Three-dimensional numerical simulation of the Kalthoff experiment. International Journal of Fracture 105 (2), 161-186.

Bever, M., Holt, D., Titchener, A., 1973. The Stored Energy of Cold Work. Pergamon Press, London.

Chichili, D.R., Ramesh, K.T., Hemker, K.J., 2004. Adiabatic shear localization in alpha-titanium: experiments, modeling and microstructural evolution. Journal of the Mechanics and Physics of Solids 52 (8), 1889-1909.

Dorogoy, A., Rittel, D., 2005. Numerical validation of the shear compression specimen (SCS). Part I: Quasi-static large strain testing. Exp. Mech. 45 (2), 167-177.

Fouvry, S., Liskiewicz, T., Kapsa, P., Hannel, S., Sauger, E., 2003. An energy description of wear mechanisms and its applications to oscillating sliding contacts. Wear 255, 287-298.

Johnson, G.R., Cook, W.H., 1985. Fracture Characteristics of 3 Metals Subjected to Various Strains, Strain Rates, Temperatures and Pressures. Engineering Fracture Mechanics 21 (1), 31-48.

Kalthoff, J.F., 1988. Shadow optical analysis of dynamic fracture. Optical Engng. 27, 835-840.

Kolsky, H., 1949. An investigation of the mechanical properties of materials at very high rates of loading. Proc. Phys. Soc. London 62-B, 676-700.

Marchand, A., Duffy, J., 1988. An experimental study of the formation process of adiabatic shear bands in a structural steel. J. Mech. Phys. Solids 36 (3), 251-283.

Mason, J.J., Rosakis, A.J., Ravichandran, G., 1994. On the strain and strain rate dependence of the fraction of plastic work converted into heat: an experimental study using high speed infrared detectors and the Kolsky bar. Mechanics of Materials 17, 135-145.

McVeigh, C., Vernerey, F., Liu, W.K., Moran, B., Olson, G., 2007. An interactive micro-void shear localization mechanism in high strength steels. Journal of the Mechanics and Physics of Solids 55 (2), 225-244.

Medyanik, S., Liu, W., Li, S., 2007. On criteria for adiabatic shear band propagation. J.Mech. Phys. Solids 55 (7), 1439-1461.

Merzer, A.M., 1982. Modelling of adiabatic shear band development from small imperfections. J. Mech. Phys. Solids 30 (5), 323-328.

Meyers, M.A., LaSalvia, J.C., Nesterenko, V.F., Chen, Y.J., Kad, B.K., 1996. Dynamic recrystallization in high strain rate deformation. In: McNelley, T.R. (Ed.), The Third International Conference on Recrystallization and Related Phenomena, pp. 279-286.

Meyers, M.A., Nesterenko, V.F., LaSalvia, J.C., Xu, Y.B., Xue, Q., 2000. Observation and modeling of dynamic recrystallization in high-strain, high strain-rate deformation of metals. J. Phys. IV France Colloq. C3 PR9, 51-56.

Molinari, A., Clifton, R.J., 1987. Analytical characterization of the shear localization in thermoviscoplastic materials J. Applied Mech. 54 (4), 806-812.

Needleman, A., Tvergaard, V., 1995. Analysis of a brittle-ductile transition under dynamic shear loading. Int. J. Solids and Structures 32 (17/18), 2571-2590.

Ravi-Chandar, K., 1995. On the failure mode transitions in polycarbonate under dynamic mixed mode loading. Int. J. Solids and Structures 32 (6/7), 925-938.

Rittel, D., 1998. The influence of temperature on dynamic failure mode transition. Mechanics of Materials 30, 217-227.

Rittel, D., 1999. The conversion of plastic work to heat during high strain rate deformation of glassy polymers. Mechanics of Materials 31 (2), 131-139.

Rittel, D., Landau, P., Venkert, A., 2008. Dynamic recrystallization as a potential cause for adiabatic shear failure. Physical Review Letters 101 (16), 165501.

Rittel, D., Lee, S., Ravichandran, G., 2002. A shear compression specimen for large strain testing. Experimental Mechanics 42 (1), 58-64.

Rittel, D., Wang, Z.G., Merzer, M., 2006. Adiabatic shear failure and dynamic stored energy of cold work. Physical Review Letters 96, 075502.

Sauger, E., Fouvry, S., Ponsonnet, L., Kapsa, P., Martin, J.M., Vincent, L., 2000. Tribologically transformed structure in fretting. Wear 245 (1-2), 39-52.

Shi, J., Liu, C.R., 2004. The influence of material models on finite element simulation of machining. Journal of Manufacturing Science and Engineering-Transactions of the Asme 126 (4), 849-857.

Taylor, G.I., Quinney, H., 1934. The latent energy remaining in a metal after cold working. Proc. Royal Soc. London 143, 307-326.

Toth, L.S., Hildenbrand, A., Molinari, A., 2000. Dynamic recrystallisation in adiabatic shear bands. J. de Phys. IV France 10, Pr9-365-370.

Tresca, H., 1879. Sur la fluidité et l'écoulement des corps solides. Annales du Conservatoire des Arts et Métiers 4.

Wang, Z., 2007. Experimental study of adiabatic shear band formation. Mechanical Engineering Dept. Technion, Haifa, p. 120.

Wright, T., 2002. The Physics and Mathematics of Adiabatic Shear Bands. Cambridge University Press, Cambridge.

Zener, C., Hollomon, J.H., 1944. Effect of strain rate upon plastic flow of steel J. Applied Phys. 15 (1), 22-32.

Zhou, M., Rosakis, A.J., Ravichandran, G., 1996a. Dynamically propagating shear bands in impact-loaded prenotched plates. II- Numerical Simulations. J. Mech. Phys. Solids 44 (6), 1007-1032.

Zhou , M., Rosakis, A.J., Ravichandran, G., 1996b. Dynamically propagating shear bands in impact-loaded prenotched plates. I- Experimental investigations of temperature signatures and propagation speed. J. Mech. Phys. Solids 44 (6), 981-1006.

Zisso, I., 2006. An investigation into the dynamic deformation and fracture of MAR250 steel. Mechanical Engineering Dept. Technion, Haifa, p. 120.

Dolinski *et al.* (2010)

Table 1: The elastic material properties, Johnson-Cook parameters (eqn. (4)), and failure criterion parameters (eqns. (2-3)) of all the four test cases.

Test case	1	2				3	4
Test type	Dyamic torsion of cylindrical specimen	Dynamic mode II fracture of a plate containing an edge crack				Axial impact of cylindrical specimen	Axial impact of an SCS specimen
Specimen material	HY-100 steel	Maraging 250 grade steel				Magnesium-Aluminum alloy (AM50)	Magnesium-Aluminum alloy (AM50)
	Elastic parameters						
E[GPa]	205	190				45	45
ν	0.28	0.3				0.35	0.35
	Plastic parameter						
	JC	Mises plasticity				JC	JC
		Yield stress [MPa]	Plastic strain	Rate $[s^{-1}]$	Temperature [^{o}C]		
B[MPa]	1067	2050	0	0	0	5000	3277
		2100	0.15	0	0		
C	0.028	2200	0	3000	0	0.015	0.015
		2250	0.15	3000	0		
m	0.7	2400	0	10000	0	0.88	0.88
		2450	0.15	10000	0		
n	0.107	1800	0	0	100	1.26	1.26
		1850	0.15	0	100		
$\dot{\varepsilon}_0[s^{-1}]$	3300	2000	0	3000	100	1	1
		2050	0.15	3000	100		
T_0 [^{o}K]	300	2200	0	10000	100	300	300
		2250	0.15	10000	100		
	Physical parameters						
ρ [Kg/m^3]	7870	8000				1770	1770
c [J/(Kg·^{o}K)]	477	450				1020	1020
β	0.9	0.9				0.9	0.9
T_m [^{o}K]	1500	not relevant				708	708
	Energy criterion parameters						
b	3	1				1	1
$W_{crit}\left[MJ/m^3\right]$	250	350				50	40
$W_{frac}\left[MJ/m^3\right]$	750	500				120	140

Table 2: Profile of the applied boundary velocity as a function of time.

Time[s]	Amplitude[m/s]
0	0
$40x10^{-6}$	7.5
$400\ x10^{-6}$	7.5
$410\ x10^{-6}$	0
$500\ x10^{-6}$	0

Table 3: Tensile stress failure as a function of the impacted velocity of Maraging 250.

V [m/s]	calculated $\dot{\varepsilon}$ $[s^{-1}]$	Tensile stress failure [MPa]
1	30-100	1900 (quasi-static)
5	101-1250	2000
17	7000-8000	3200
18	7300-8500	3300
25	10000-23000	4000

Table 4: Profile of the applied boundary velocity as a function of time, cylindrical specimen.

Time[s]	Amplitude[m/s]
0	0
$5x10^{-6}$	10
$75\ x10^{-6}$	10
$80\ x10^{-6}$	0
$200\ x10^{-6}$	0

Table 5: Profile of the applied boundary velocity as a function of time, shear compression specimen.

Time[s]	Amplitude[m/s]
0	0
$10x10^{-6}$	25
$100\ x10^{-6}$	25
$110\ x10^{-6}$	0
$200\ x10^{-6}$	0

FIGURES

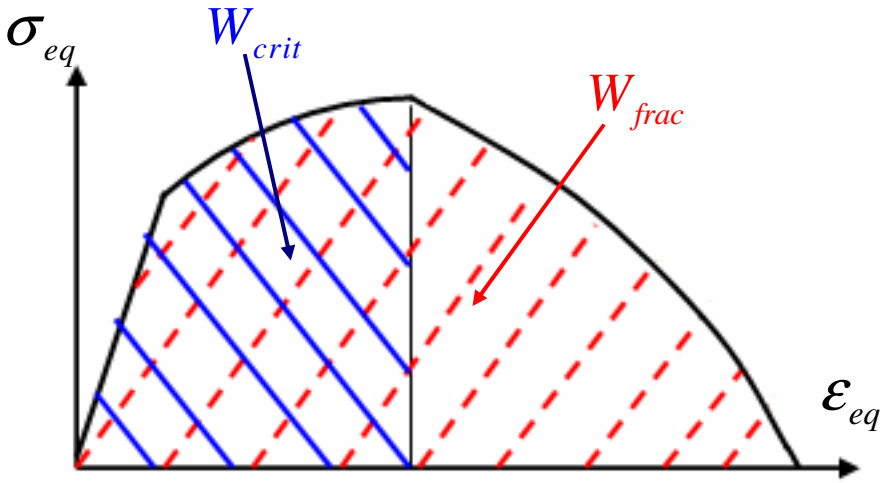

Figure 1: Schematic stress strain curve with the failure criterion used throughout this work.

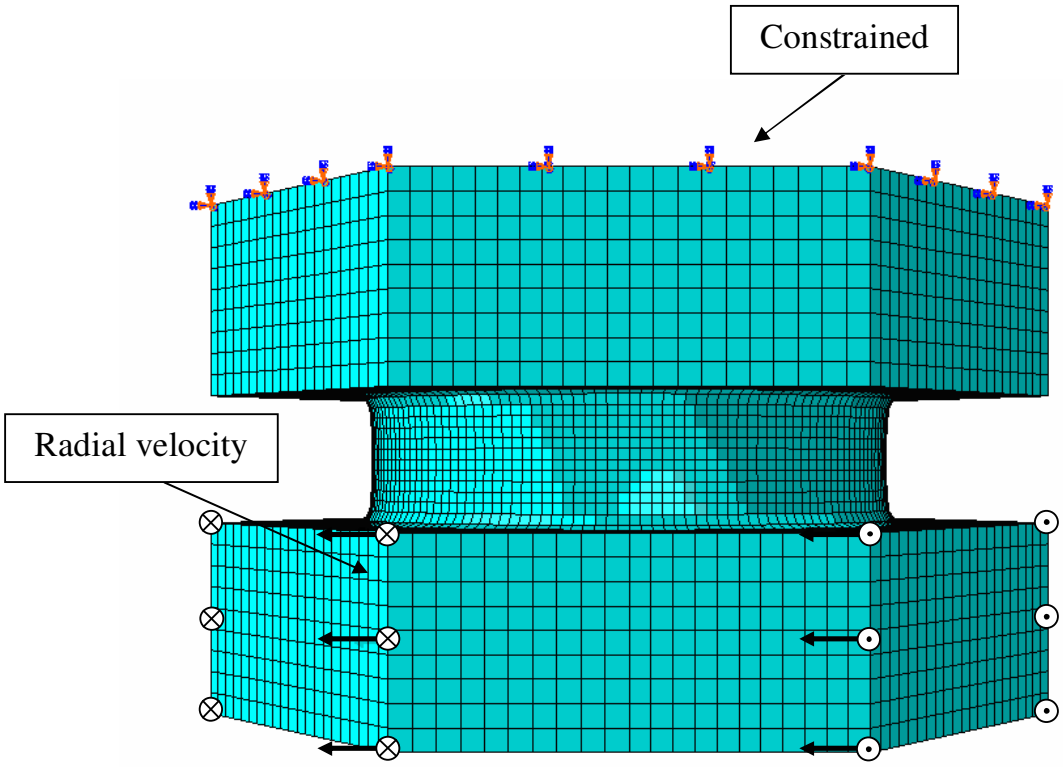

Figure 2: Specimens boundary conditions and mesh. Velocity is prescribed on one end while the other is constrained.

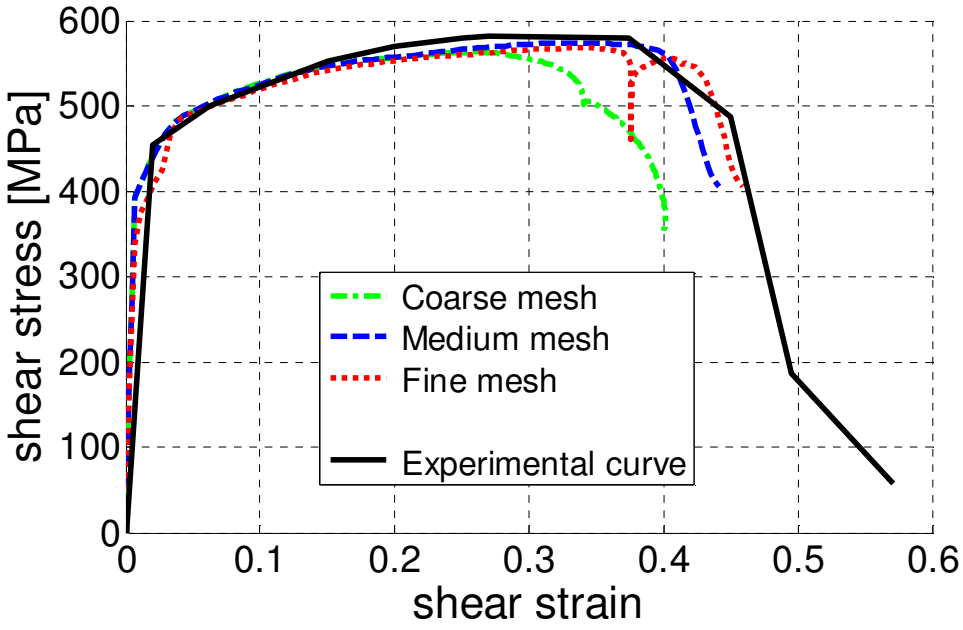

Figure 3: Average shear stress – shear strain curves for three different mesh sizes and an experimental curve. Note that the medium and fine mesh sizes yield similar results, which serves as a qualitative benchmark for mesh size selection.

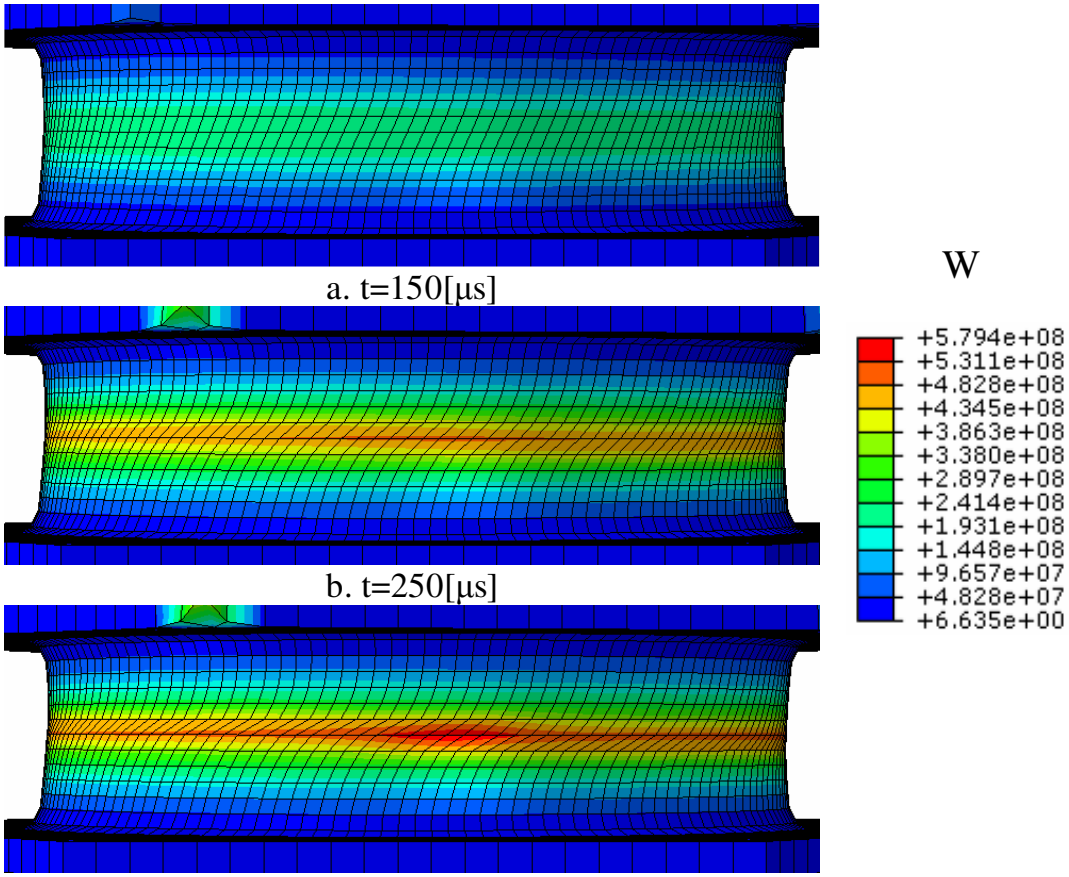

Figure 4: Deformed gauge section and strain energy density W at various time intervals. a. At t=150[μs]. b. At t=250[μs]. c. At t=280[μs]. Note the sharpening of the localization.

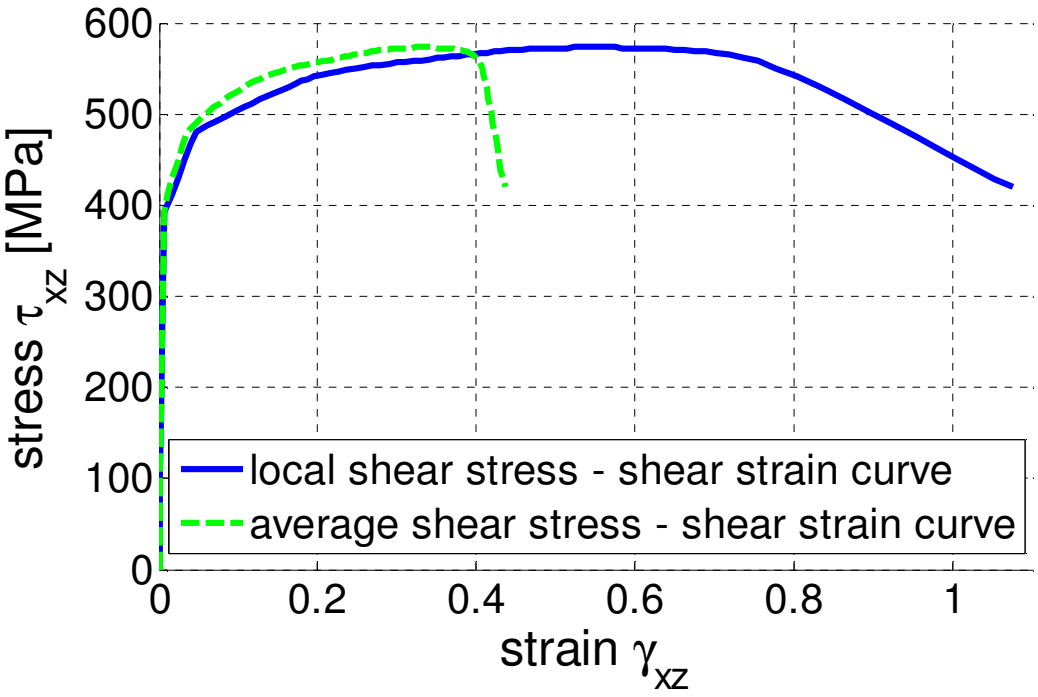

Figure 5: Local and averaged shear stress–shear strain curves. Averaging is carried out throughout the gauge section while the local curves are taken from the bottom of the groove (center of the shear band).

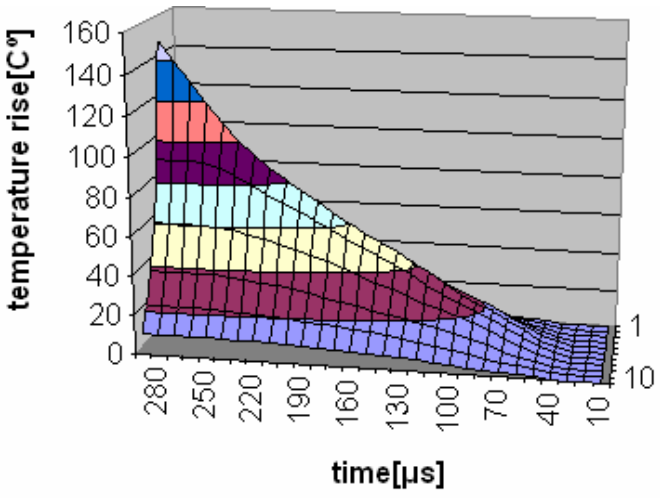

a.

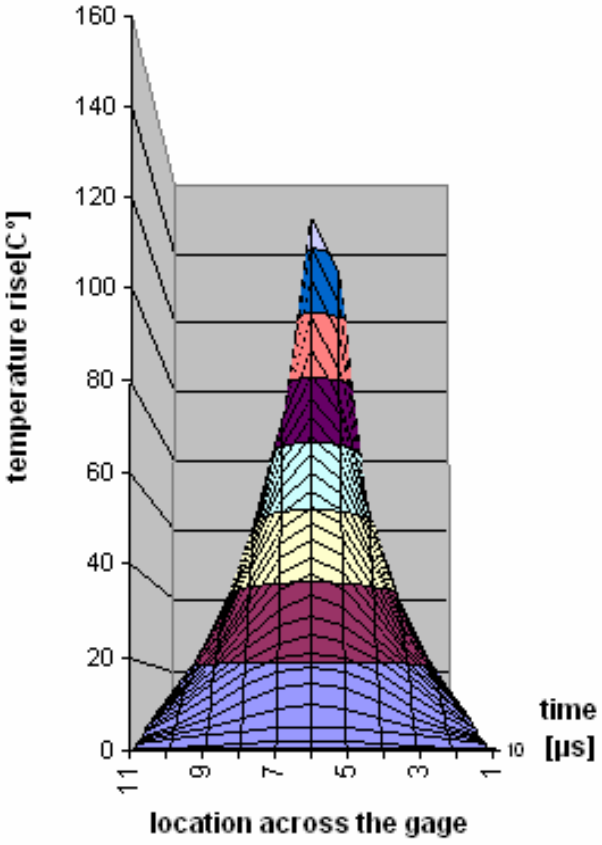

b.

Figure 6: The temperature on the surface of the gauge as a function of time and position across the gauge section. a. A 3D view. b. location-temperature view. Note the steep change of slope starting at t=230[µs], at which the failure criterion is just fulfilled.

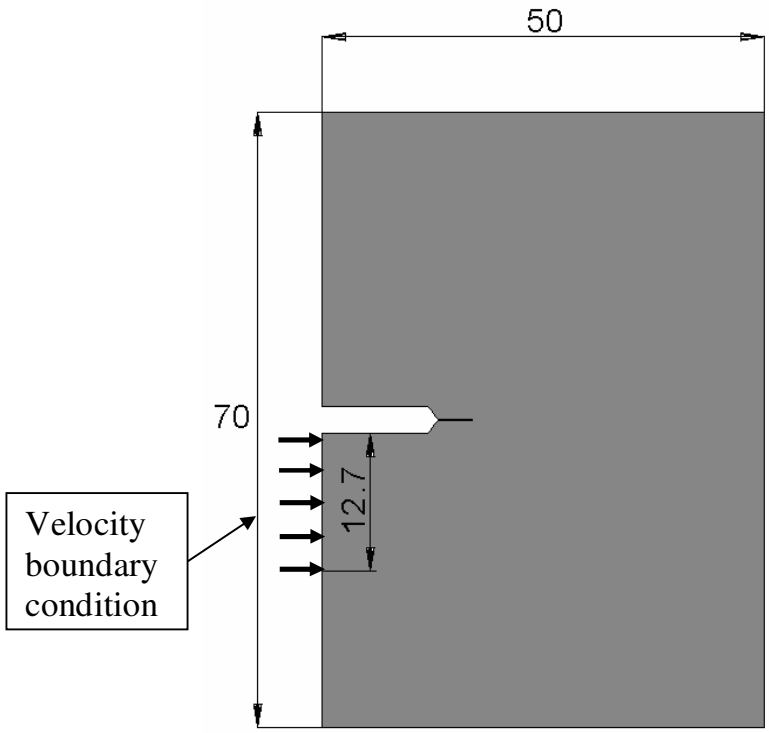

a.

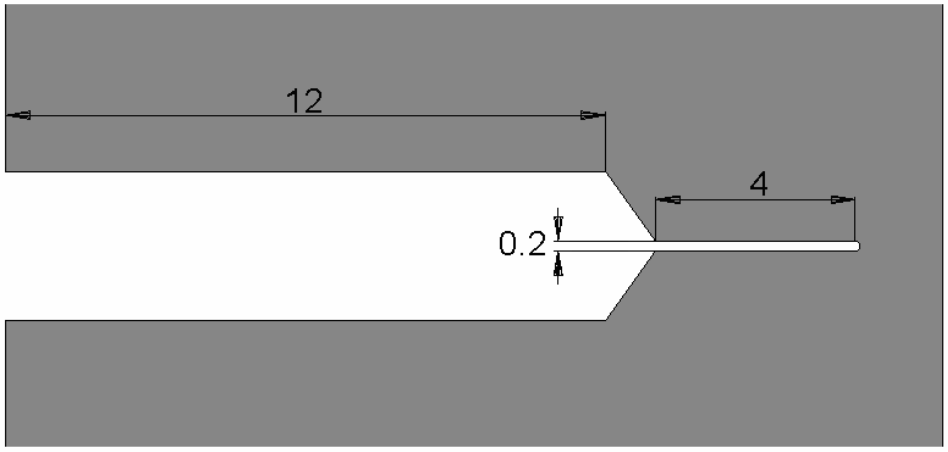

b.

Figure 7: Specimen's geometry, dimensions and boundary conditions. a. is the whole specimen with the velocity boundary condition. b. is the notch's shape and dimensions. All dimensions are in millimeters.

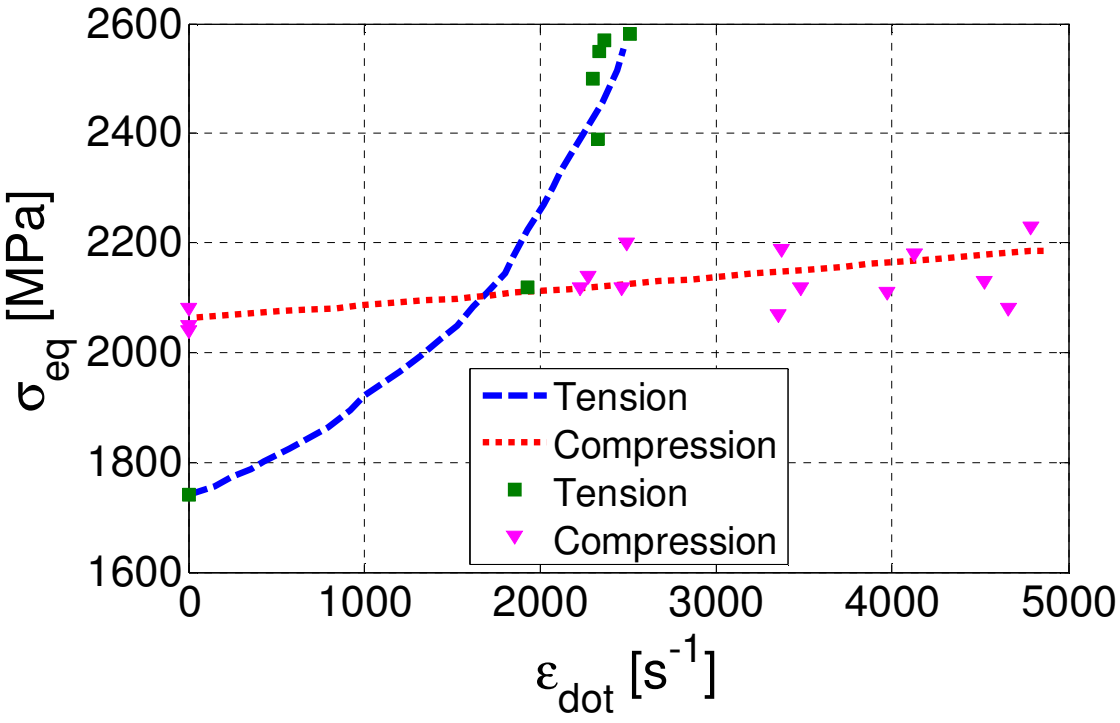

Figure 8: Flow stress at $\varepsilon = 0.06$ for dynamic tension and compression tests of Maraging 250 steel at various strain rates (Zisso, 2006).

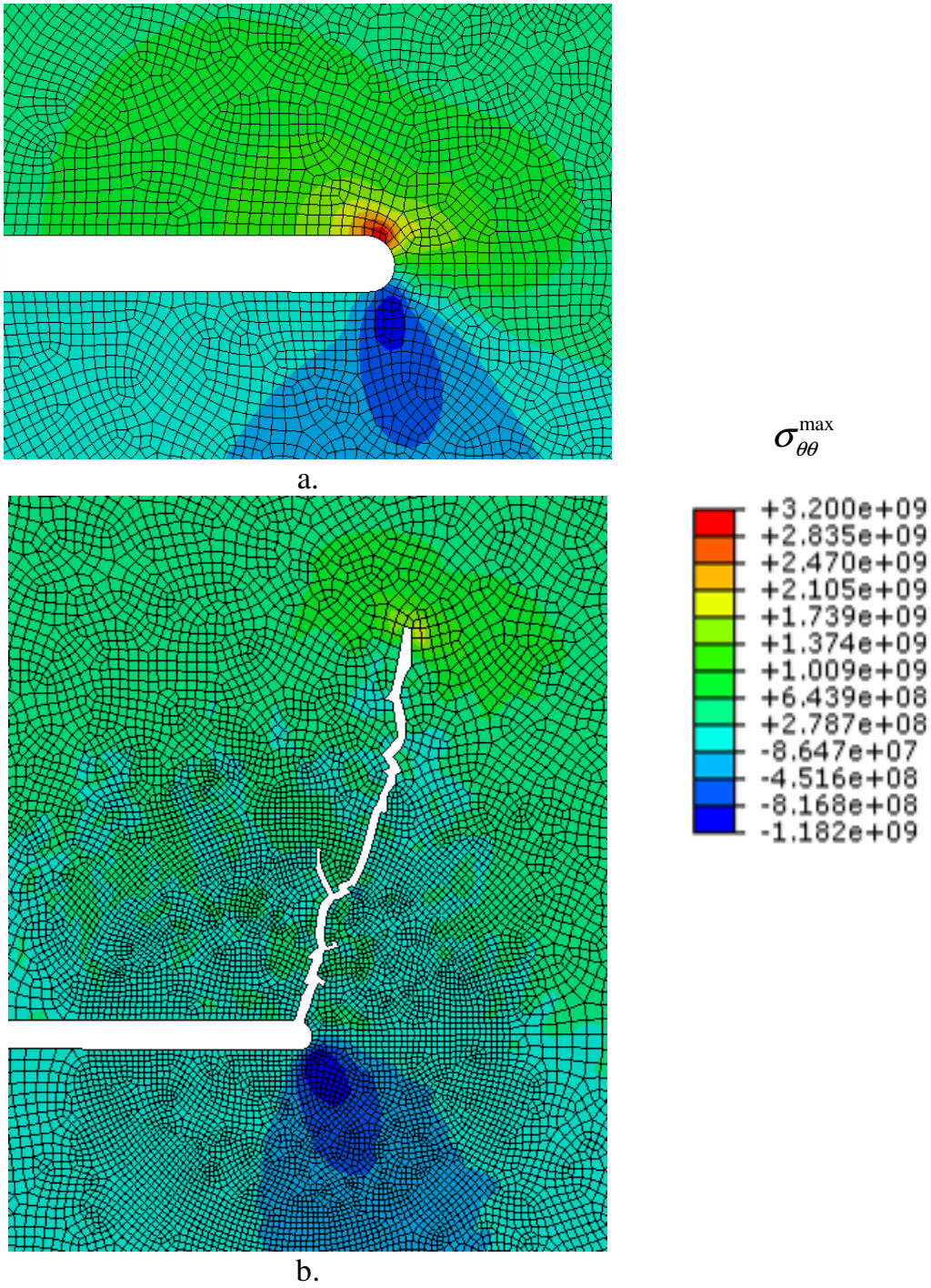

Figure 9: The plate's maximal principal stress at times of a. t=10[μs] and b. t=12[μs], impact velocity of 17[m/s]. It can be seen that at time of $t \approx 11$[μs] a crack starts to propagate. The maximal value of the principal stress is the tensile stress criterion for this impact velocity - 3200[MPa].

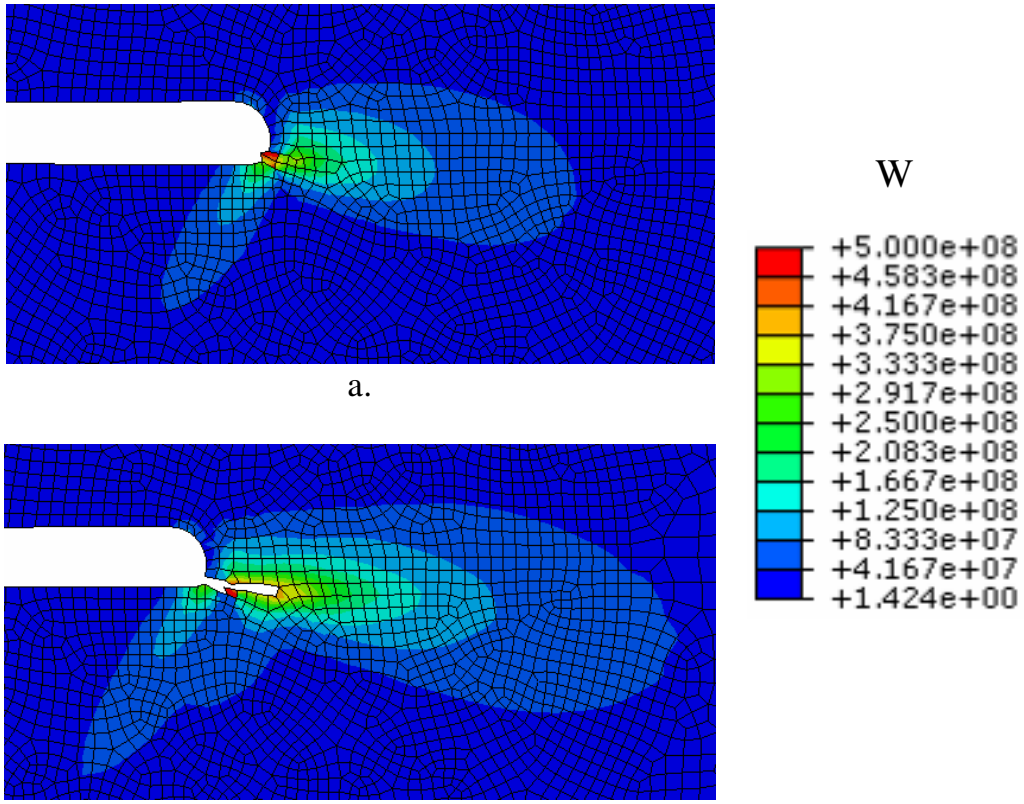

Figure 10: Strain energy density at times of: a. t=18[μs] and b. t=20[μs], impact velocity of 18[m/s]. The highest value in the map of strain energy density is the value of the energy criterion - $500[MJ/m^3]$.

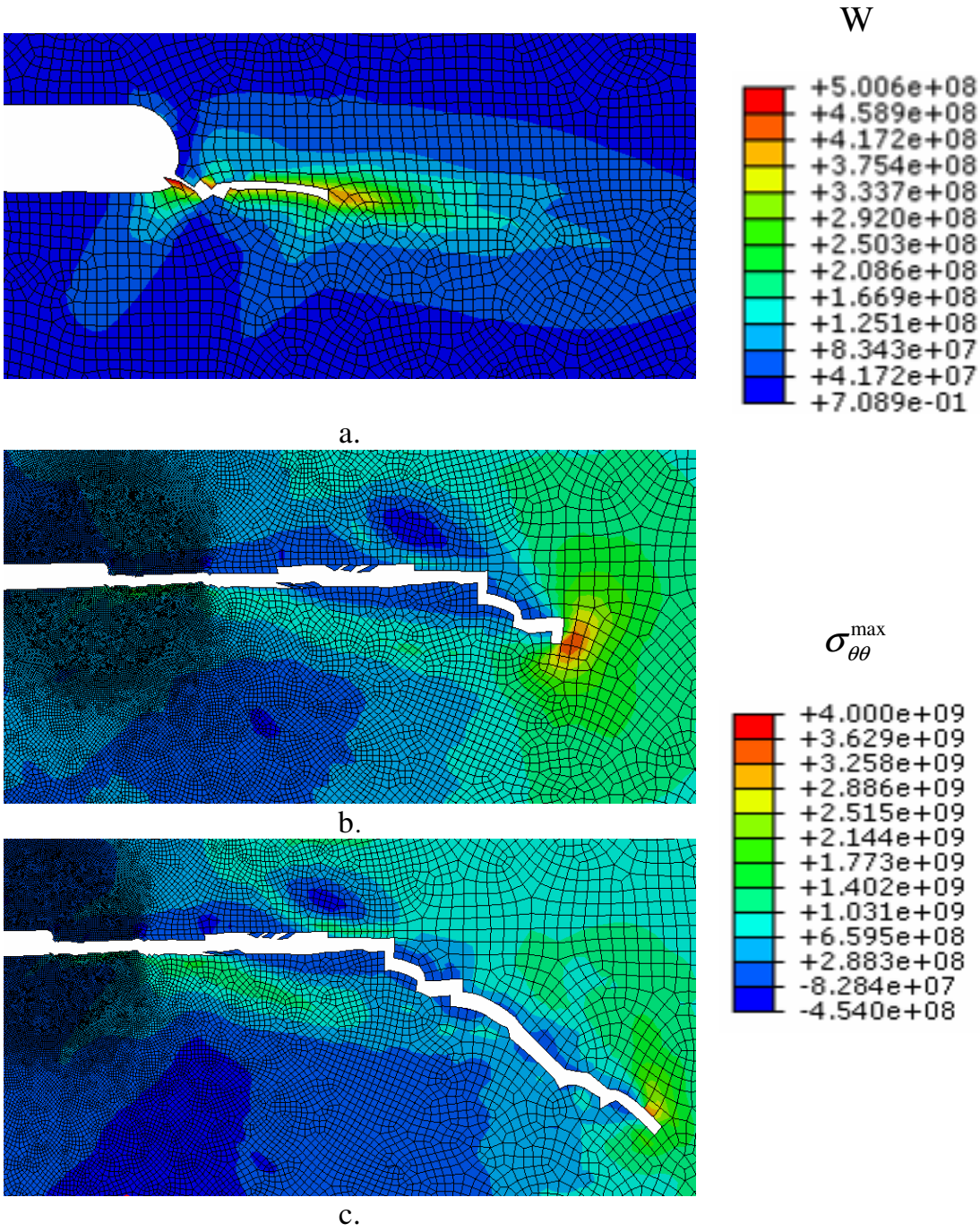

Figure 11: Fracture path at various times for an impact velocity of 25[m/s]. a. Failure is initially ductile at t=13[μs]. b. At t≈70[μs] the failure becomes brittle, and an opening crack is clearly visible at t=75[μs] (this view), forming an angle of -30° with the initial failure path c. At t=77[μs] the opening crack grows. Note the maximal value of the stress map, 4000[MPa], which corresponds to the critical value for the applied velocity of 25[m/s].

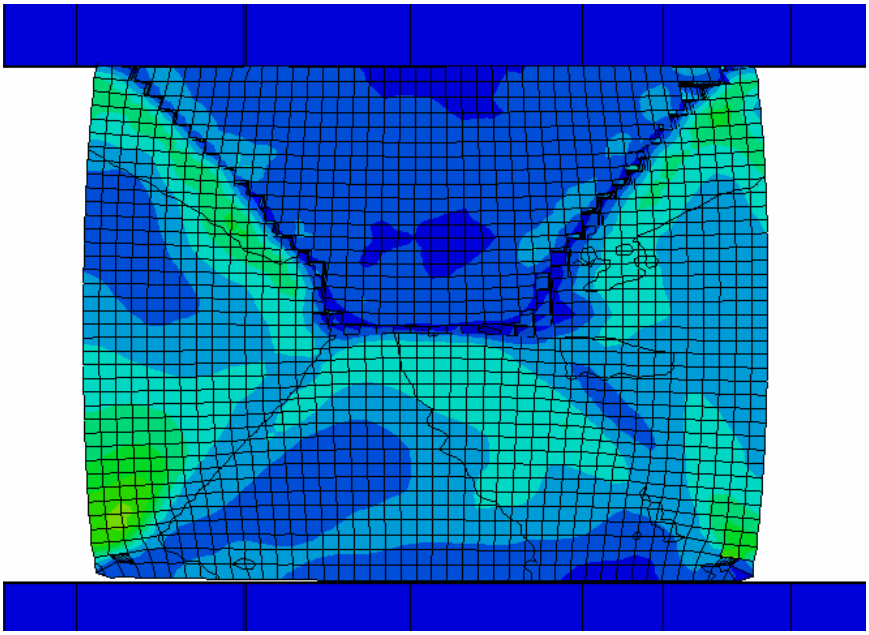

a.

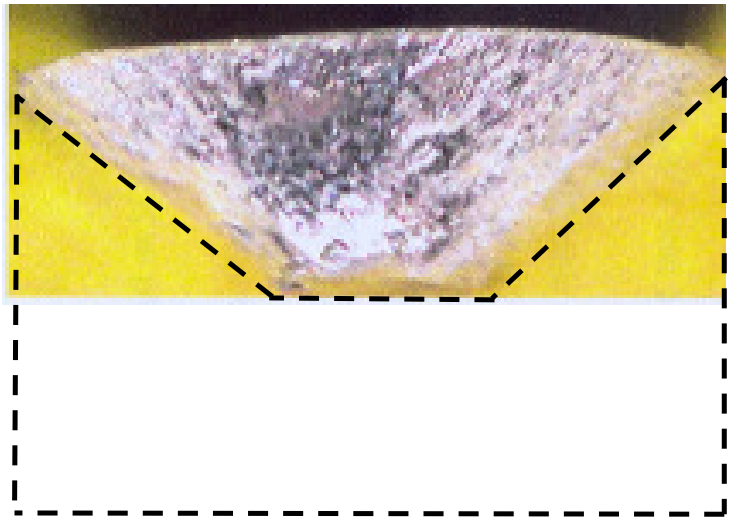

b.

Figure 12: Cylinder fracture pattern. a. Mises stress distribution (absolute values not shown) at t=107[μs]. Elements are erased in the cone fracture and the stresses are very low in its vicinity. b. Cup & cone fracture plane caused by ASB in AM50 cylindrical specimen. Reprinted from Rittel, et al. (2006).

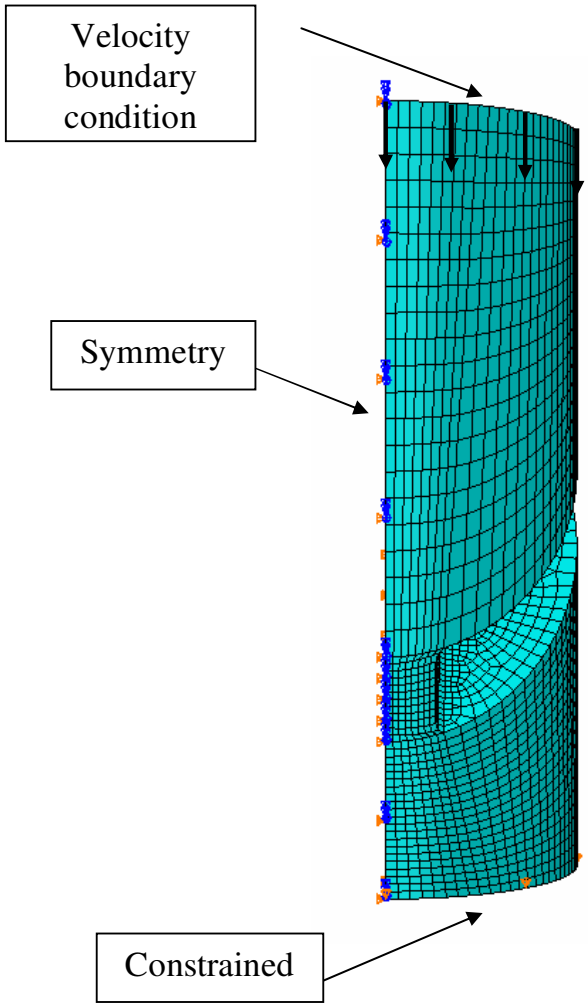

Figure 13: Shear compression specimen's boundary conditions and mesh. The specimen is symmetrical so that only half of it is modeled. The bottom surface is fully constrained and a velocity boundary condition is applied on upper surface.

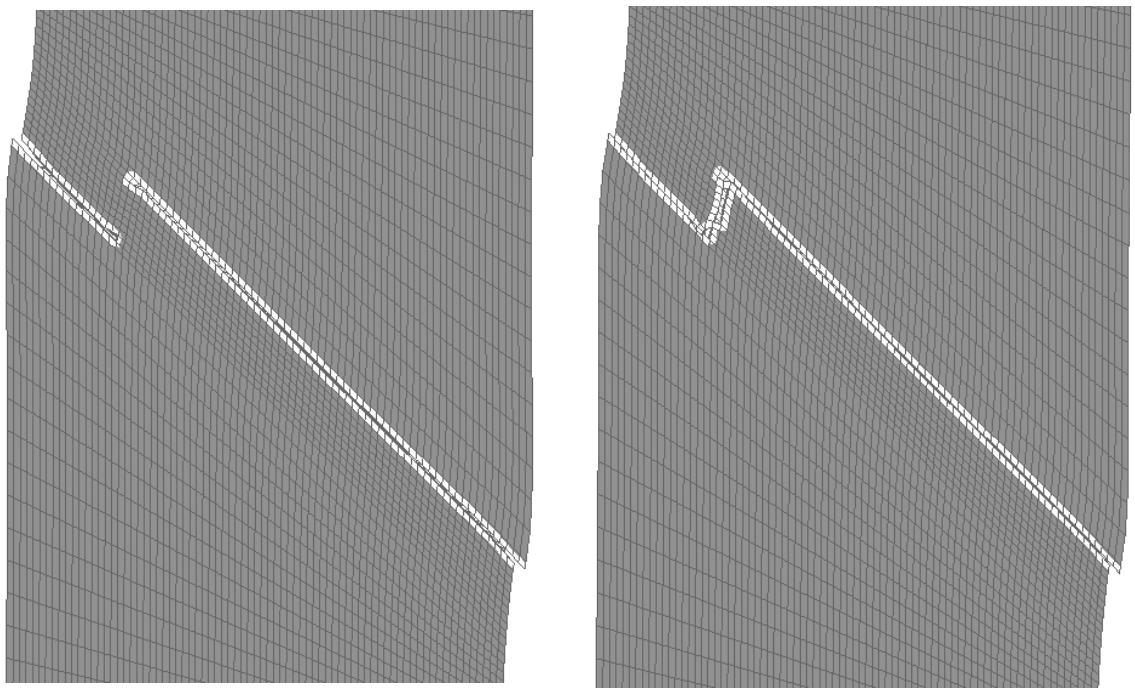

a. b.

Figure 14: Failure path on the specimen. a. t=45[μs], two shear bands propagate in each fillet, just before total fracture. b. t=47[μs], the two shear bands are bridged by a short slant fracture, causing full specimen failure.

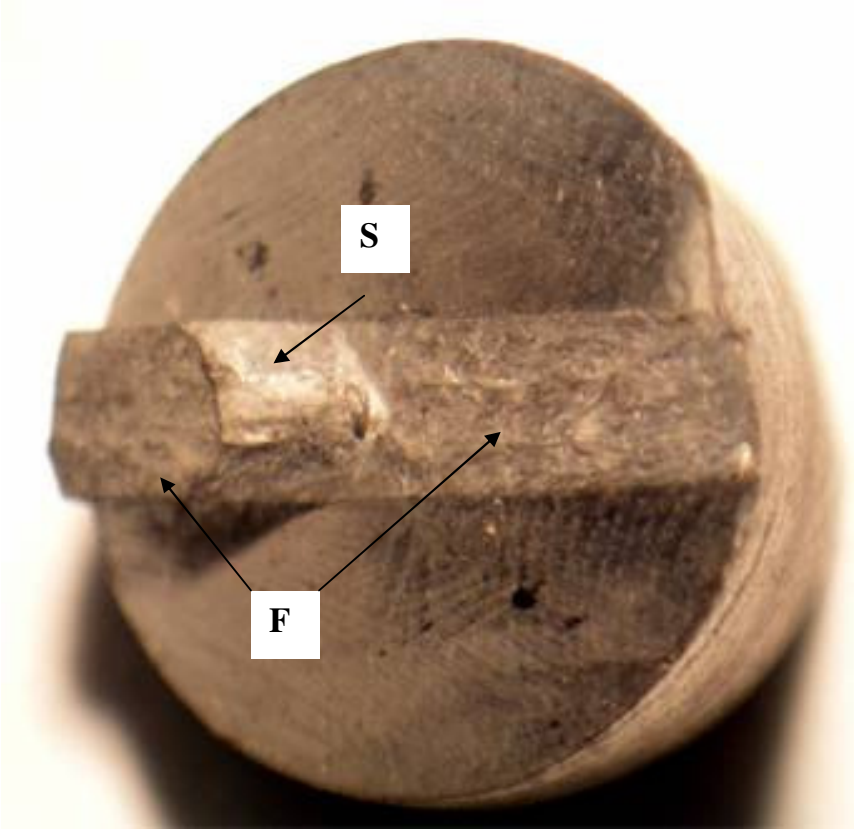

Figure 15: Fractured SCS specimen. Two cracks develop in the fillets (F), which are connected by a slant segment (S).